Editors' Suggestion | Featured in Physics

Local Readout and Control of Current and Kinetic Energy Operators in Optical Lattices

Alexander Impertro, Simon Karch, Julian F. Wienand, SeungJung Huh, Christian Schweizer, Immanuel Bloch, and Monika Aidelsburger

Fakultät für Physik, Ludwig-Maximilians-Universität, 80799 Munich, Germany;
Max-Planck-Institut für Quantenoptik, 85748 Garching, Germany;
and Munich Center for Quantum Science and Technology (MCQST), 80799 Munich, Germany

(Received 9 January 2024; revised 17 May 2024; accepted 6 June 2024; published 5 August 2024)

Quantum gas microscopes have revolutionized quantum simulations with ultracold atoms, allowing one to measure local observables and snapshots of quantum states. However, measurements so far were mostly carried out in the occupation basis. Here, we demonstrate how all kinetic operators, such as kinetic energy or current operators, can be measured and manipulated with single-bond resolution. Beyond simple expectation values of these observables, the single-shot measurements allow one to access full counting statistics and complex correlation functions. Our work paves the way for the implementation of efficient quantum state tomography and hybrid quantum computing protocols for itinerant particles on a lattice. In addition, we demonstrate how site-resolved programmable potentials enable a spatially selective, parallel readout in different bases as well as the engineering of arbitrary initial states.

DOI: 10.1103/PhysRevLett.133.063401

Analog quantum simulators offer a promising route toward practical quantum advantage [1–4]. Among those, neutral atoms in optical lattices are ideal candidates for simulating a large variety of condensed matter models [5,6], providing access to single-atom- and single-site-resolved detection of (nonlocal) correlation functions and counting statistics through quantum gas microscopy [7–9]. However, most measurements in these platforms so far were carried out in the occupation basis, limiting the range of state preparation and readout protocols that can be implemented. A measurement of the current operator would, for example, aid in the study of nonequilibrium dynamics by allowing one to probe information scrambling through bond-resolved local currents and off-diagonal correlations [10,11], as well as in the simulation of interacting topological phases that host equilibrium currents [12,13]. Furthermore, a measurement in a complete basis would enable the implementation of Hamiltonian learning, which is a promising approach to benchmark analog quantum simulators [14–18].

In this Letter, we demonstrate how—in addition to the density—the kinetic energy and the current operators, or any linear combination of the two ("kinetic operators"), can be measured and controlled with local resolution using optical superlattices [19,20]. Optical superlattices enable parallel high-fidelity nearest-neighbor manipulations, which have been used, e.g., to generate a large number of entangled atom pairs based on controlled collisions and exchange interactions [21–25]. The idea behind our scheme is to use superlattices to project a many-body system onto a two-dimensional (2D) lattice of isolated double wells (DWs), as depicted in Fig. 1(a). The sites of the DW form a two-level system, where the tunnel coupling J and a potential energy difference Δ can be interpreted as Pauli X and Z operations [Fig. 1(b)]. This has been used in earlier experiments to measure a spatially averaged current operator [26] and spin currents [27]. In this Letter we extend these ideas and combine them with local resolution and manipulation techniques. We further demonstrate arbitrary rotations in the DWs by combining X and Z operations [Fig. 1(c)]. This is used to measure kinetic operators with local resolution and in a single experimental realization, providing access to correlations and counting statistics [28]. Additionally, we apply site-resolved programmable potentials to perform coherent spatially selective basis rotations and engineer states with variable density patterns, which can also be used to generate various phase patterns or coherent superpositions. Our technique is directly applicable to interacting quantum systems given that interactions can be switched off during the DW manipulations, as has been demonstrated in a number of experiments, where atomic beam splitter operations have been used to extract information about particle-number statistics, indistinguishability, or the second-order Rényi entropy [29–33].

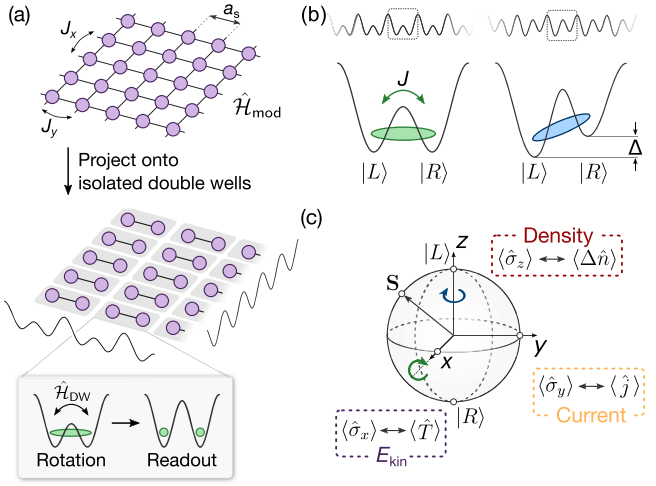

FIG. 1. Programmable rotations using double-well potentials. (a) After evolving with a Hubbard Hamiltonian $\hat{\mathcal{H}}_{\mathrm{mod}}$, the system is projected onto isolated double wells, where programmable local operations are applied before readout according to $\hat{\mathcal{H}}_{\mathrm{DW}}$ [defined in the main text and (b)], which rotates the measurement basis. The occupation in the DWs is then frozen and read out with local resolution. (b) Atomic operations in a DW potential, forming a two-level system out of the states $|L\rangle$ and $|R\rangle$. A symmetric DW with tunnel coupling J realizes an X rotation (left), while a strong tilt Δ implements a Z rotation (right). (c) The rotations are used to map current $\hat{j}$ and kinetic energy $\hat{T}$ onto density imbalance $\Delta\hat{n}$ for readout, so that all Bloch-vector components $\mathbf{S} = (\hat{\sigma}_x, \hat{\sigma}_y, \hat{\sigma}_z)$ are accessible.

Experimental scheme—We create an optical superlattice potential by superimposing a short and a long wavelength lattice with a wavelength ratio of 2, realizing a periodic array of tunable DWs [Fig. 1(b)] [20]. For a deep long-period lattice, the inter-DW coupling is negligible and the states $|L\rangle$ and $|R\rangle$ in each DW form a two-level system with the Hamiltonian $\hat{\mathcal{H}}_{\mathrm{DW}} = -J\hat{\sigma}_x - (\Delta/2)\hat{\sigma}_z$, where $\hat{\sigma}_i$ ($i = \{x, y, z\}$) are the Pauli operators. For symmetric DWs ($\Delta = 0$), an X rotation is realized [Fig. 1(b), left], while a strongly tilted, decoupled DW ($\Delta \gg J$) implements a Z rotation [Fig. 1(b), right].

Local site-resolved densities $\langle\hat{n}_{L,R}\rangle$ are directly accessible in experiments. Here, $\hat{n}_i = \hat{a}_i^\dagger\hat{a}_i$ is the bosonic number operator and $\hat{a}_i^\dagger$ is the bosonic creation operator for the state i ($i = \{L, R\}$). A measurement in the Z basis corresponds to probing the density difference within one DW, i.e., $\Delta\hat{n} = \hat{n}_L - \hat{n}_R = \hat{\sigma}_z$. In contrast, the Y basis encodes the local current between the two wells, defined for a Hubbard model with real-valued tunneling J as $\hat{j} = iJ(\hat{a}_R^\dagger\hat{a}_L - \hat{a}_L^\dagger\hat{a}_R) = J\hat{\sigma}_y$ [26,28]. Similarly, the X basis corresponds to the kinetic energy $\hat{T} = -J(\hat{a}_R^\dagger\hat{a}_L + \hat{a}_L^\dagger\hat{a}_R) = -J\hat{\sigma}_x$.

To measure the kinetic operators, we use the DW dynamics to map them onto density imbalance $\Delta\hat{n}$. As illustrated in Fig. 1(c), the current can be mapped onto the density via an $X_{\pi/2}$ rotation [i.e., rotating for a time $\tilde{t} = h/(8J)$, with h Planck's constant], giving $\langle\Delta\hat{n}\rangle = -\langle\hat{j}\rangle/J$, and the kinetic energy by concatenating a $Z_{\pi/2}$ [rotating for $\tilde{t} = h/(4\Delta)$] and an $X_{\pi/2}$ rotation as $\langle\Delta\hat{n}\rangle = -\langle\hat{T}\rangle/J$ [cf. Fig. 2(e), derivation in Supplemental Material [34]]. This realizes a single-shot readout of the density, kinetic energy, and current with local resolution.

Results—The experimental sequence starts by loading ultracold cesium atoms into a 2D optical lattice that consists of a superlattice along x and a single-color lattice along y, leading to an array of DWs along x [35,36]. The initial state is a product state, with one particle per isolated DW prepared in $|L\rangle$. We obtain a maximum imbalance $\mathcal{I} = (n_L - n_R)/(n_L + n_R)$ of typically 0.93(4) (see Supplemental Material [34] for details).

We implement X rotations by suddenly lowering the short lattice depth. As shown in Fig. 2(a), we find imbalance oscillations corresponding to a tunnel coupling $J = h \times 484.3(5)$ Hz, an experimental π time $t_\pi^{(\mathrm{exp})} = 449(3)$ μs (taking into account the finite ramp time), and a $1/e$ decay constant $\tau = 57(13)$ ms. Using the decay envelope, we estimate the fidelity of a single X_π pulse as $\mathcal{F} = 99.2(2)\%$ (see Supplemental Material [34] for details). This fidelity is mostly limited by spatially inhomogeneous potential energy variations that detune the DWs locally and modify the oscillation frequency according to $f = \sqrt{4J^2 + \Delta^2}/h$.

Next, we demonstrate Z rotations using a Ramsey sequence. After an $X_{\pi/2}$ pulse, we jump the superlattice phase away from the symmetric configuration, causing the Bloch vector to rotate on the equator as the superposition of $|L\rangle$ and $|R\rangle$ time evolves in the tilted DW potential [cf. Fig. 1(b)]. This evolution is probed using a second $X_{\pi/2}$ pulse, yielding oscillations that reveal the rotation of the state vector along the equator [Fig. 2(b)]. The oscillations correspond to a tilt of $\Delta = h \times 2.406(5)$ kHz and exhibit a damping that is consistent with an on-site white noise disorder uniformly distributed in $[-W, W]$ of amplitude $W = h \times 49(2)$ Hz (see Supplemental Material [34] for details). The envelope can also be approximated by a single exponential, giving a T_2^* time of 6(1) ms ($1/e$ decay).

Here, dephasing occurs faster compared to X rotations, as local potential variations modify the tilt linearly, in contrast to the quadratic correction for X rotations. To cancel the dephasing due to static disorder, we employ a spin-echo sequence as shown in Fig. 2(c). We determine a T_2 time of 113(10) ms [Fig. 2(d)], corresponding to around 270 cycles on the equator at the previously measured Δ. The T_2 time is more than an order of magnitude larger than the T_2^* decay of the Ramsey signal and confirms that the dephasing is dominated by static potential inhomogeneities (see Supplemental Material [34] for an estimate of a residual slowly varying disorder).

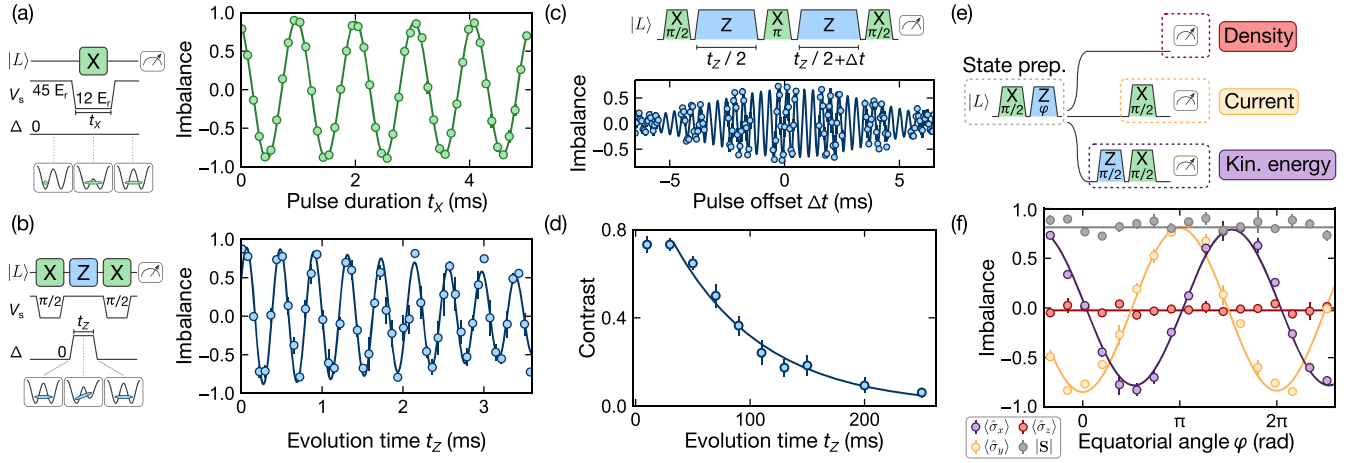

FIG. 2. Global double-well operations and rotations of the measurement basis. (a) X rotation starting with the DWs initialized in $|L\rangle$. V_s denotes the depth of the short lattice, which sets the tunnel coupling J inside the well. The solid line is a fit to an exponentially damped sine. (b) Measurement of a Z rotation using a Ramsey sequence. The solid line is a fit to a numerical model accounting for on-site potential disorder (see Supplemental Material [34] for details). The nonzero initial phase of the oscillations in (a) and (b) stems from the finite ramp times of V_s and Δ. (c) Spin-echo sequence. Example trace for $t_Z = 30$ ms, recorded by varying the time offset Δt in the second Z rotation. The solid line is a sine fit with a Gaussian envelope function. (d) Measurement of the T_2 time using the spin-echo sequence. For each data point, the imbalance contrast was evaluated by varying the pulse offset and fitting the resulting imbalance oscillation. The solid line represents an exponential fit to the data that omit the initial data point, from which we derive T_2 as the duration at which the contrast decreases to $1/e$ of its initial value. The error bars are the standard errors of the fit. (e) Scheme to determine the density, current, and kinetic energy of the states lying on the equator of the Bloch sphere. (f) Measurement result as a function of the equatorial angle φ. The solid lines for the current (yellow) and the kinetic energy (purple) are fits to a sine. The solid line for the density is a fit to a constant function. The gray data points show the length of the Bloch vector $|\mathbf{S}|$, which averages to 0.81(6) (solid gray line). The zero of the horizontal axis has been calibrated on the first minimum of the $\hat{\sigma}_y$ trace.

Next, we perform a global measurement of equatorial states of the form $(|L\rangle + e^{i(\varphi+\pi/2)}|R\rangle)/\sqrt{2}$ in all three Pauli bases [Fig. 2(e)]. The states are prepared by concatenating an $X_{\pi/2}$ pulse and a Z pulse of variable duration to tune the equatorial angle φ. We then measure all three components of the Bloch vector $\mathbf{S} = (\hat{\sigma}_x, \hat{\sigma}_y, \hat{\sigma}_z)$. As expected, we find that $\langle\hat{\sigma}_z\rangle = 0$ and is time independent [Fig. 2(f)], while the expectation value of the current $\hat{\sigma}_y$ and the kinetic energy $\hat{\sigma}_x$ show high contrast oscillations with a relative phase shift of $\pi/2$. The measured average length of the Bloch vector $|\mathbf{S}| = \sqrt{\langle\hat{\sigma}_x\rangle^2 + \langle\hat{\sigma}_y\rangle^2 + \langle\hat{\sigma}_z\rangle^2}$ is 0.81(6), which is mostly limited by the Z rotation used for state preparation.

We extend the global manipulations demonstrated above with local control using a digital micromirror device (DMD) to project programmable repulsive potentials and locally tilt selected DWs. As an example, we perform global X rotations and simultaneously tilt every other DW [Fig. 3(a)]. The tilted DWs indeed oscillate at a higher frequency and smaller amplitude, as expected from detuned Rabi oscillations. The maximum possible tilt is limited by the available power of the DMD light and the resolution, which causes light to spill over to adjacent sites, hence reducing the differential tilt. A spatially resolved evaluation reveals that local manipulations can be realized in parallel over extended regions of the system (see panel on right-hand side of Fig. 3(a)].

The DMD addressing further enables locally programmable Z rotations, which we demonstrate with a Ramsey-type sequence [Fig. 3(b)]. To this end, we locally imprint a π relative phase via a Z_π rotation on every other DW. Scanning the duration of the first X pulse results in strong out-of-phase oscillations with a fitted phase shift of $\Phi = 1.04(2)\pi$. This demonstrates a local rotation of the measurement basis, paving the way toward measurements of more complex observables, such as correlators between current and kinetic energy.

Local rotations can also be used for precise, coherent engineering of spatially structured initial states. As an example, we use locally detuned X rotations, where the tilt value is chosen such that a minimum in the detuned DW imbalance coincides with a maximum in the bare DWs [e.g., around $t_X = 1.3$ ms in Fig. 3(a), see Supplemental Material [34] for details on the sequence]. Choosing this point, we can coherently transfer an initial $|\ldots10101010\ldots\rangle$ state to $|\ldots01100110\ldots\rangle$ (here, the notation refers to the occupation of the underlying short lattice structure, i.e., $|L\rangle = |10\rangle$, $|R\rangle = |01\rangle$). In Fig. 3(c), this is demonstrated using a DMD mask that is translationally invariant in the direction perpendicular to the DWs. The average occupation [Fig. 3(d)] indicates a filling of 86(4)% in the occupied, and 7(2)% in the empty stripes, which is close to the initial-state quality, suggesting a high preparation fidelity (see Supplemental Material [34] for details on the initial state).

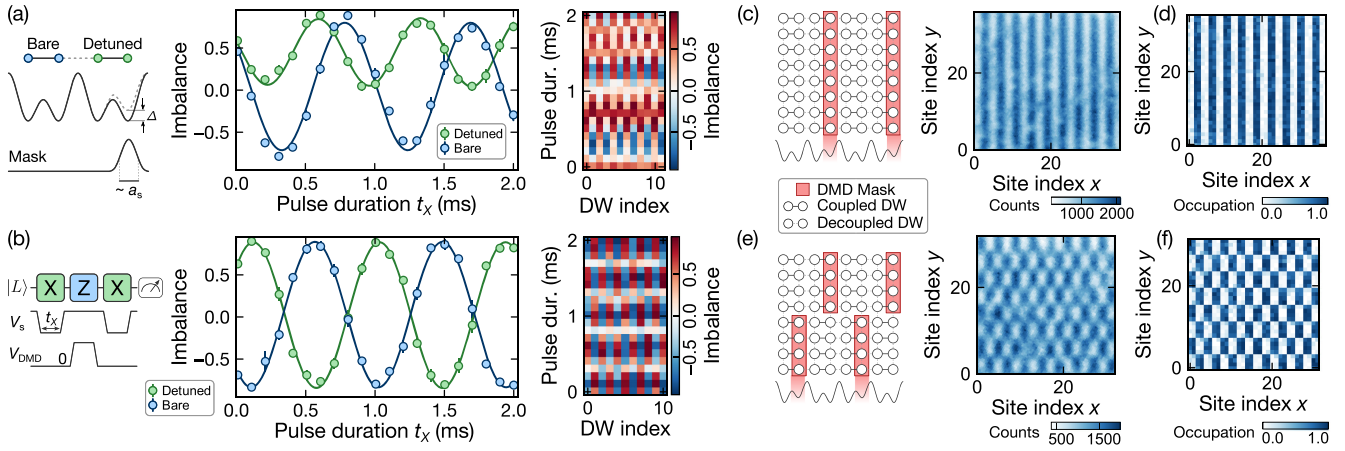

FIG. 3. Local programmable double-well operations. (a) Locally detuned X rotations. Using a digital micromirror device, we project a repulsive potential that locally tilts every other DW in a one-dimensional (1D) superlattice potential. The DMD mask consists of bright stripes with a width of $0.6a_s$, which is broadened by the point-spread function to $\sim$1–2a_s. The solid lines are fits to a sine, yielding a differential tilt of $\Delta = h \times 797(13)$ Hz. Right: spatially resolved oscillation, averaged over the perpendicular direction. (b) Local Z rotations, implemented by tilting every other DW along a 1D chain. The Z pulse area was chosen to be around π, which is visualized by scanning the duration of the first X pulse, resulting in out-of-phase imbalance oscillations. The solid lines are fits to a sine, yielding a relative phase shift of $1.04(2)\pi$. Evaluation details as in (a). (c) State engineering using locally detuned DW oscillations with the programmed mask shown on the left (the red shading marks the sites that are lifted in energy). The panel on the right shows a single fluorescence image of the resulting state with alternating pairs of empty and occupied rows. (d) Averaged occupation for the state in (c). (e) State engineering in 2D (mask on the left), resulting in a checkerboardlike state of 4×2 site blocks. The panel on the right shows a single fluorescence image. (f) Averaged occupation for the state in (e).

Similarly, we can choose a DMD mask that has an alternating pattern in the direction perpendicular to the DWs. This realizes a checkerboardlike state made up of (4×2)-site blocks [Figs. 3(e) and 3(f)] with similar average fillings of 84(5)% in the occupied blocks and 8(3)% in the empty blocks. The attainable preparation fidelities are mostly limited by the resolution and alignment of the DMD imaging system, which is particularly challenging due to our rather small lattice spacing of $a_s = 383.5$ nm. Even higher fidelities could easily be achieved for larger lattice spacings or higher imaging resolution.

Finally, we would like to highlight that the single-shot and locally resolved nature of the presented measurements furthermore enable the extraction of correlation functions. This is crucial, for example, when spatial features are not stationary between individual shots. To demonstrate this capability, we prepare a 2D lattice of isolated symmetric DWs with complex-valued tunnel couplings $Je^{i\varphi_{i,j}}$; here (i, j) labels the DW location in the 2D lattice. The spatially varying phases $\varphi_{i,j}$ are realized using a laser-assisted tunneling scheme based on a 1D running-wave lattice (see Supplemental Material [34] and Refs. [37–39] for details). We prepare a single particle in the ground state of each DW, i.e., $|\psi\rangle_{i,j} = (|L\rangle + e^{i\varphi_{i,j}}|R\rangle)/\sqrt{2}$. For the experimental geometry chosen in this Letter, the phase $\varphi_{i,j}$ increases by about $\pi/2$ per bond in both spatial directions [see Fig. 4(a)].

To resolve the local phase $\varphi_{i,j}$ and its spatial dependence, we measure the expectation value of the current operator $\hat{j}_{i,j}$, which is given for a DW at location (i, j) by $\langle \hat{j}_{i,j} \rangle / J = \sin \varphi_{i,j}$. However, while the laser-assisted tunneling scheme fixes the periodicity of the phase distribution $\varphi_{i,j}$, there is a global phase shift φ_0 between the pattern and the underlying lattice, which varies randomly between different experimental realizations. As a consequence, the expectation value of the current operator vanishes [Fig. 4(b)]. Nonetheless, the phase pattern can be detected by evaluating the connected 2D current-current correlation function $C^c_{x,y} = \langle \hat{j}_{i,j} \hat{j}_{i+d_x,j+d_y} \rangle - \langle \hat{j}_{i,j} \rangle \langle \hat{j}_{i+d_x,j+d_y} \rangle$.

Figure 4(c) shows the experimentally measured 2D correlation function (left panel), which, focusing on small distances ($d_{x,y} \lesssim 4$), matches our expectation given the phase pattern in Fig. 4(a). For larger distances, we find Moiré fringes, which arise from a slight angular misalignment between the lattice base vectors and the running-wave lattice. The resulting phase pattern hence does not evolve exactly by a factor of $\pi/2$ between neighboring bonds. As can be seen in Fig. 4(c) (middle and right panels), we find excellent agreement with a theoretical model that accounts for relative angles (see Supplemental Material [34] for further details on the fitting model). The measured correlator amplitude is around 78% of the ideal value, which we believe to be mostly limited by an imperfect adiabatic ground-state preparation.

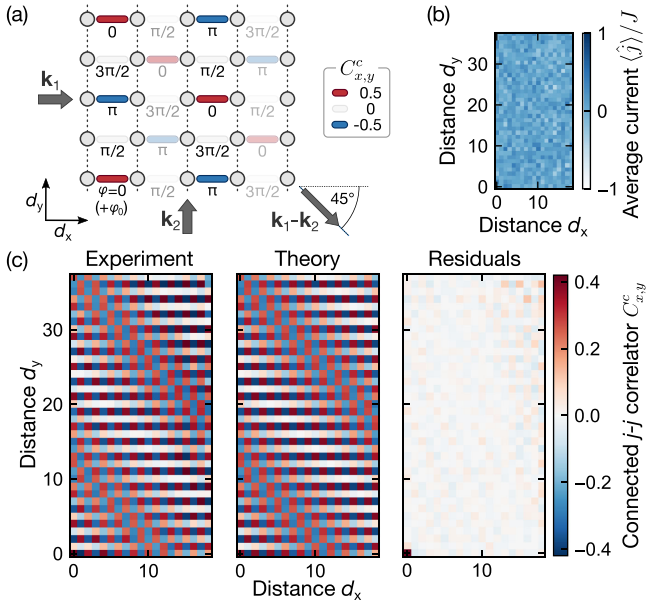

FIG. 4. Resolving spatially varying complex tunnel couplings using current-current correlations. (a) Scheme to generate spatially varying tunnel coupling phases using a running-wave modulation created from the interference of two laser beams with wave vectors $\mathbf{k}_{1,2}$, giving a $\pi/2$-advancing phase pattern with random global phase offset φ_0. The color coding on the bonds illustrates the expected current-current correlation with respect to the bond at (0,0). Because of the projection onto isolated DWs, only every second phase in the x direction is accessible (light shading). (b) Averaged current signal, calculated from 50 realizations. (c) Measured 2D connected current-current correlator evaluated from 50 averages (left), fit to a theoretical model (middle), and fit residuals (right). The fit yields an amplitude of $A = 0.777(3)$, a common-mode angle between the laser-assisted tunneling beams and the lattice of $\theta_c = 1.802(3)°$ as well as a relative angle deviation from 90° of $\theta_r = -0.558(8)°$, where the uncertainties denote the standard errors of the fit (see Supplemental Material [34] for details).

Conclusion—We have demonstrated how optical superlattices can be used to enhance the capabilities of quantum gas microscopes through spatially resolved single-shot measurements of kinetic operators. This will be essential for the detection of exotic many-body states with trivial signatures in density observables, such as strongly interacting topological phases with equilibrium currents [12,13,28]. In addition, local manipulations can be used to engineer tailored initial states to study initial-state dependent thermalization in the presence of constraints, e.g., in the context of Hilbert-space fragmentation [40–42] or lattice gauge theories [6,43–46]. Moreover, local manipulation of the measurement basis can be used to enhance the measurement sensitivity for metrology applications [47], as well as to access further nontrivial observables [48] and correlators, e.g., between current and kinetic energy.

The fidelity of local rotations can be further enhanced using composite pulse sequences [49–51]. This paves the way for the implementation of efficient quantum state tomography schemes [52–57], lattice-based quantum computing protocols [25], measurements of the (many-body) energy spectrum [58,59], Hamiltonian learning [14,16–18], and hybrid quantum computing approaches, such as variational algorithms [60–64].

Acknowledgments—The authors would like to acknowledge insightful discussions with Eugene Demler, Jens Eisert, Manuel Endres, Timon Hilker, and Michael Knap. Furthermore, we would like to thank Ignacio Pérez, Scott Hubele, and Sophie Häfele for technical contributions to the experimental apparatus. We received funding from the Deutsche Forschungsgemeinschaft (DFG, German Research Foundation) via Research Unit FOR5522 under Project No. 499180199, via Research Unit FOR 2414 under Project No. 277974659, and under Germany's Excellence Strategy—EXC-2111–390814868 and from the German Federal Ministry of Education and Research via the funding program quantum technologies—from basic research to market (Contract No. 13N15895 FermiQP). This publication has further received funding under Horizon Europe program HORIZON-CL4-2022-QUANTUM-02-SGA via the Project No. 101113690 (PASQuanS2.1). J. F. W. acknowledges support from the German Academic Scholarship Foundation and the Marianne-Plehn-Program. S. H. was supported by the education and training program of the Quantum Information Research Support Center, funded through the National research foundation of Korea (NRF) by the Ministry of science and ICT (MSIT) of the Korean government (No. 2021M3H3A1036573). C. S. has received funding from the European Union's Framework Programme for Research and Innovation Horizon 2020 under the Marie Skłodowska-Curie Grant Agreement No. 754388 (LMUResearchFellows) and from LMUexcellent, funded by the BMBF and the Free State of Bavaria under the Excellence Strategy of the German Federal Government and the Länder.

Data availability—The data that supports the figures and plots of the main text can be found in [65].

[1] J. I. Cirac and P. Zoller, Nat. Phys. **8**, 264 (2012).
[2] J. Preskill, Quantum **2**, 79 (2018).
[3] R. Trivedi, A. F. Rubio, and J. I. Cirac, arXiv:2212.04924.
[4] A. J. Daley, I. Bloch, C. Kokail, S. Flannigan, N. Pearson, M. Troyer, and P. Zoller, Nature (London) **607**, 667 (2022).
[5] C. Gross and I. Bloch, Science **357**, 995 (2017).
[6] J. C. Halimeh, M. Aidelsburger, F. Grusdt, P. Hauke, and B. Yang, arXiv:2310.12201.

[7] W. S. Bakr, J. I. Gillen, A. Peng, S. Fölling, and M. Greiner, Nature (London) **462**, 74 (2009).
[8] J. F. Sherson, C. Weitenberg, M. Endres, M. Cheneau, I. Bloch, and S. Kuhr, Nature (London) **467**, 68 (2010).
[9] C. Gross and W. S. Bakr, Nat. Phys. **17**, 1316 (2021).
[10] B. Swingle, G. Bentsen, M. Schleier-Smith, and P. Hayden, Phys. Rev. A **94**, 040302(R) (2016).
[11] A. Bohrdt, C. B. Mendl, M. Endres, and M. Knap, New J. Phys. **19**, 063001 (2017).
[12] M. Piraud, F. Heidrich-Meisner, I. P. McCulloch, S. Greschner, T. Vekua, and U. Schollwöck, Phys. Rev. B **91**, 140406(R) (2015).
[13] B. Wang, X. Dong, and A. Eckardt, SciPost Phys. **12**, 095 (2022).
[14] N. Wiebe, C. Granade, C. Ferrie, and D. G. Cory, Phys. Rev. Lett. **112**, 190501 (2014).
[15] M. Holzäpfel, T. Baumgratz, M. Cramer, and M. B. Plenio, Phys. Rev. A **91**, 042129 (2015).
[16] J. Wang, S. Paesani, R. Santagati, S. Knauer, A. A. Gentile, N. Wiebe, M. Petruzzella, J. L. O'Brien, J. G. Rarity, A. Laing, and M. G. Thompson, Nat. Phys. **13**, 551 (2017).
[17] J. Carrasco, A. Elben, C. Kokail, B. Kraus, and P. Zoller, PRX Quantum **2**, 010102 (2021).
[18] W. Yu, J. Sun, Z. Han, and X. Yuan, Quantum **7**, 1045 (2023).
[19] J. Sebby-Strabley, M. Anderlini, P. S. Jessen, and J. V. Porto, Phys. Rev. A **73**, 033605 (2006).
[20] S. Fölling, S. Trotzky, P. Cheinet, M. Feld, R. Saers, A. Widera, T. Müller, and I. Bloch, Nature (London) **448**, 1029 (2007).
[21] M. Anderlini, P. J. Lee, B. L. Brown, J. Sebby-Strabley, W. D. Phillips, and J. V. Porto, Nature (London) **448**, 452 (2007).
[22] S. Trotzky, P. Cheinet, S. Fölling, M. Feld, U. Schnorrberger, A. M. Rey, A. Polkovnikov, E. A. Demler, M. D. Lukin, and I. Bloch, Science **319**, 295 (2008).
[23] S. Trotzky, Y.-A. Chen, U. Schnorrberger, P. Cheinet, and I. Bloch, Phys. Rev. Lett. **105**, 265303 (2010).
[24] B. Yang, H. Sun, C.-J. Huang, H.-Y. Wang, Y. Deng, H.-N. Dai, Z.-S. Yuan, and J.-W. Pan, Science **369**, 550 (2020).
[25] W.-Y. Zhang *et al.*, Phys. Rev. Lett. **131**, 073401 (2023).
[26] M. Atala, M. Aidelsburger, M. Lohse, J. T. Barreiro, B. Paredes, and I. Bloch, Nat. Phys. **10**, 588 (2014).
[27] C. Schweizer, M. Lohse, R. Citro, and I. Bloch, Phys. Rev. Lett. **117**, 170405 (2016).
[28] S. Keßler and F. Marquardt, Phys. Rev. A **89**, 061601(R) (2014).
[29] J. Sebby-Strabley, B. L. Brown, M. Anderlini, P. J. Lee, W. D. Phillips, J. V. Porto, and P. R. Johnson, Phys. Rev. Lett. **98**, 200405 (2007).
[30] A. M. Kaufman, B. J. Lester, C. M. Reynolds, M. L. Wall, M. Foss-Feig, K. R. A. Hazzard, A. M. Rey, and C. A. Regal, Science **345**, 306 (2014).
[31] R. Islam, R. Ma, P. M. Preiss, M. Eric Tai, A. Lukin, M. Rispoli, and M. Greiner, Nature (London) **528**, 77 (2015).
[32] A. M. Kaufman, M. E. Tai, A. Lukin, M. Rispoli, R. Schittko, P. M. Preiss, and M. Greiner, Science **353**, 794 (2016).
[33] G.-X. Su, H. Sun, A. Hudomal, J.-Y. Desaules, Z.-Y. Zhou, B. Yang, J. C. Halimeh, Z.-S. Yuan, Z. Papić, and J.-W. Pan, Phys. Rev. Res. **5**, 023010 (2023).
[34] See Supplemental Material at http://link.aps.org/supplemental/10.1103/PhysRevLett.133.063401 for details on the experimental setup, calibrations and benchmarks as well as more detailed derivations.
[35] A. Impertro, J. F. Wienand, S. Häfele, H. von Raven, S. Hubele, T. Klostermann, C. R. Cabrera, I. Bloch, and M. Aidelsburger, Commun. Phys. **6**, 166 (2023).
[36] J. F. Wienand, S. Karch, A. Impertro, C. Schweizer, E. McCulloch, R. Vasseur, S. Gopalakrishnan, M. Aidelsburger, and I. Bloch, arXiv:2306.11457.
[37] M. Aidelsburger, M. Atala, S. Nascimbène, S. Trotzky, Y.-A. Chen, and I. Bloch, Phys. Rev. Lett. **107**, 255301 (2011).
[38] H. Miyake, G. A. Siviloglou, C. J. Kennedy, W. C. Burton, and W. Ketterle, Phys. Rev. Lett. **111**, 185302 (2013).
[39] M. E. Tai, A. Lukin, M. Rispoli, R. Schittko, T. Menke, D. Borgnia, P. M. Preiss, F. Grusdt, A. M. Kaufman, and M. Greiner, Nature (London) **546**, 519 (2017).
[40] S. Moudgalya, A. Prem, R. Nandkishore, N. Regnault, and B. A. Bernevig, in *Memorial Volume for Shoucheng Zhang* (World Scientific, Singapore, 2020), pp. 147–209.
[41] P. Sala, T. Rakovszky, R. Verresen, M. Knap, and F. Pollmann, Phys. Rev. X **10**, 011047 (2020).
[42] V. Khemani, M. Hermele, and R. Nandkishore, Phys. Rev. B **101**, 174204 (2020).
[43] E. Zohar, J. I. Cirac, and B. Reznik, Rep. Prog. Phys. **79**, 014401 (2016).
[44] M. Dalmonte and S. Montangero, Contemp. Phys. **57**, 388 (2016).
[45] M. C. Bañuls *et al.*, Eur. Phys. J. D **74**, 165 (2020).
[46] M. Aidelsburger *et al.*, Phil. Trans. R. Soc. A **380**, 20210064 (2022).
[47] A. L. Shaw, R. Finkelstein, R. B.-S. Tsai, P. Scholl, T. H. Yoon, J. Choi, and M. Endres, Nat. Phys. **20** (2024).
[48] G. Semeghini, H. Levine, A. Keesling, S. Ebadi, T. T. Wang, D. Bluvstein, R. Verresen, H. Pichler, M. Kalinowski, R. Samajdar, A. Omran, S. Sachdev, A. Vishwanath, M. Greiner, V. Vuletić, and M. D. Lukin, Science **374** (2021).
[49] S. Wimperis, J. Magn. Reson., Ser. A **109**, 221 (1994).
[50] H. K. Cummins, G. Llewellyn, and J. A. Jones, Phys. Rev. A **67**, 042308 (2003).
[51] H. L. Gevorgyan and N. V. Vitanov, Phys. Rev. A **104**, 012609 (2021).
[52] K. Vogel and H. Risken, Phys. Rev. A **40**, 2847 (1989).
[53] M. Cramer, M. B. Plenio, S. T. Flammia, R. Somma, D. Gross, S. D. Bartlett, O. Landon-Cardinal, D. Poulin, and Y.-K. Liu, Nat. Commun. **1**, 149 (2010).
[54] D. Gross, Y.-K. Liu, S. T. Flammia, S. Becker, and J. Eisert, Phys. Rev. Lett. **105**, 150401 (2010).
[55] J.-H. Zheng, B. Irsigler, L. Jiang, C. Weitenberg, and W. Hofstetter, Phys. Rev. A **101**, 013631 (2020).
[56] S. N. Hearth, M. O. Flynn, A. Chandran, and C. R. Laumann, arXiv:2311.09291.
[57] A. Prakash and B. H. Madhusudhana, arXiv:2311.03452.
[58] P. Roushan *et al.*, Science **358**, 1175 (2017).
[59] Z.-C. Xiang, K. Huang, Y.-R. Zhang, T. Liu, Y.-H. Shi, C.-L. Deng, T. Liu, H. Li, G.-H. Liang, Z.-Y. Mei, H. Yu,

G. Xue, Y. Tian, X. Song, Z.-B. Liu, K. Xu, D. Zheng, F. Nori, and H. Fan, Nat. Commun. **14**, 5433 (2023).
[60] A. Peruzzo, J. McClean, P. Shadbolt, M.-H. Yung, X.-Q. Zhou, P. J. Love, A. Aspuru-Guzik, and J. L. O'Brien, Nat. Commun. **5**, 4213 (2014).
[61] J. R. McClean, J. Romero, R. Babbush, and A. Aspuru-Guzik, New J. Phys. **18**, 023023 (2016).
[62] A. Michel, S. Grijalva, L. Henriet, C. Domain, and A. Browaeys, Phys. Rev. A **107**, 042602 (2023).
[63] R. d. Keijzer, O. Tse, and S. Kokkelmans, Quantum **7**, 908 (2023).
[64] D. González-Cuadra, D. Bluvstein, M. Kalinowski, R. Kaubruegger, N. Maskara, P. Naldesi, T. V. Zache, A. M. Kaufman, M. D. Lukin, H. Pichler, B. Vermersch, J. Ye, and P. Zoller, Proc. Natl. Acad. Sci. U.S.A. **120**, 2304294120 (2023).
[65] A. Impertro *et al.*, Local readout and control of current and kinetic energy operators in optical lattices (2024), 10.17617/3.GELG53.
[66] T. Klostermann, C. R. Cabrera, H. von Raven, J. F. Wienand, C. Schweizer, I. Bloch, and M. Aidelsburger, Phys. Rev. A **105**, 043319 (2022).

End Matter

Appendix—The superlattice potential realized in the experiment can be described by $V_{\mathrm{sl}}(x) = V_{\mathrm{s}}\cos^2(k_{\mathrm{s}}x) + V_{\mathrm{l}}\cos^2(k_{\mathrm{l}}x + \phi_{\mathrm{sl}}/2)$ [20]. Here $V_{\mathrm{s(l)}}$ is the lattice depth, $k_{\mathrm{s(l)}} = \pi/a_{\mathrm{s(l)}}$ is the wave vector of the short-period (long-period) lattice [with $a_{\mathrm{s(l)}}$ being the lattice constant of the short-period (long-period) lattice, where $a_{\mathrm{s}} = 383.5\ \mathrm{nm} = a_{\mathrm{l}}/2$] and ϕ_{sl} is the superlattice phase. Further information about the experimental apparatus is available in Supplemental Material [34] and in earlier work [35,36,66].

For the initial-state preparation, we load a Mott-insulating state with one particle in each double well. At the end of the loading ramp, both short lattices (x, y) are at a depth of $45E_{\mathrm{r,s}}$ and the long lattice in x is at a depth of $45E_{\mathrm{r,l}}$ [$E_{\mathrm{r,s(l)}} = h^2/(8ma_{\mathrm{s(l)}}^2)$ is the recoil energy of the short (long) lattice, h is Planck's constant, and m is the atomic mass of cesium].

To implement an X rotation, the short lattice in the x direction is lowered to $12E_{\mathrm{r,s}}$ in 200 μs. After a variable hold time, the short lattice depth is increased back to $45E_{\mathrm{r,s}}$ with the same ramp duration.

To implement a Z rotation, we work in a regime where the two wells of each DW are approximately isolated ($J \approx 0$) and then jump the superlattice phase away from the symmetric point to the target tilt Δ over 100 μs using a feed-forward trick (see Supplemental Material [34] for details). After a variable hold time, the phase jump is inverted back to the symmetric configuration. Note that following each jump, the tilt needs around 500 μs to fully stabilize.

For the measurement of the current-current correlator in Fig. 4, we used the following sequence: We first prepare the same initial state as in the previous experiments, i.e., a 2D lattice of isolated DWs, each filled with one particle localized in $|L\rangle$. The superlattice phase is chosen to realize a tilt of $\Delta \approx 4.2$ kHz. Next, the short lattice in the x direction is decreased to $9E_{\mathrm{r,s}}$ over 100 ms. This realizes a bare tunnel coupling of $J \approx h \times 650$ Hz, but the particle mostly stays localized in $|L\rangle$ since $\Delta \gg J$. We then adiabatically ramp up the strength of the running-wave lattice to an induced coupling magnitude of around $h \times 150$ Hz, where the frequency difference of the individual laser beams is set equal to the DW energy gap. At this point, each double well will be in its respective single-particle ground state together with a complex phase factor that depends on its location in the lattice. To resolve the phase distribution, we perform a current measurement, which is initiated by suddenly switching off the running-wave modulation, isolating the wells by increasing the short lattice along x to $30E_{\mathrm{r,s}}$ over 500 μs and simultaneously moving the superlattice phase to the symmetric point using the feed-forward trick. Immediately after, the measurement basis is rotated by evolving in symmetric, coupled DWs to realize a rotation of $X_{\pi/2}$.

Table I shows details on the averaging and region of interest (ROI) used for evaluation of the different subfigures in the main text. Unless otherwise noted, the error bars are the standard error of the mean.

TABLE I. Details on the averaging and region of interest (ROI) used for evaluation of the different subfigures in the main text.

Figures	ROI	Repetitions
2(a)	28×32	6
2(b)	16×30	4
2(c), 2(d)	40×40	5
2(e)	18×36	3
3(a), 3(b)	24×24	3
3(d), 3(f)	...	30